## Ultrasound-assisted biofabrication and bioprinting of preferentially aligned threedimensional cellular constructs

# Parth Chansoria<sup>1,2</sup>, Lokesh Karthik Narayanan<sup>1,2</sup>, Karl Schuchard<sup>1,2</sup>, and Rohan Shirwaiker<sup>1,2,3,4</sup>

- <sup>1</sup> Edward P. Fitts Department of Industrial and Systems Engineering, North Carolina State University, Raleigh, NC 27695, United States of America
- <sup>2</sup> Comparative Medicine Institute, North Carolina State University, Raleigh, NC 27695, United States of America
- <sup>3</sup> Joint Department of Biomedical Engineering, North Carolina State University and University of North Carolina at Chapel Hill, Raleigh, NC 27695, United States of America
- <sup>4</sup> Author to whom correspondence should be addressed.

Email: rashirwaiker@ncsu.edu

**Keywords:** Biofabrication, Bioprinting, Ultrasound, Standing Bulk Acoustic Wave, 3D Acoustic Patterning, 3D Cell Manipulation, Tissue Engineering

#### Abstract

A critical consideration in tissue engineering is to recapitulate the microstructural organization of native tissues that is essential to their function. Scaffold-based techniques have focused on achieving this via the contact guidance principle wherein topographical cues offered by scaffold fibers direct migration and orientation of cells to govern subsequent cell-secreted extracellular matrix organization. Alternatively, approaches based on acoustophoretic, electrophoretic, photophoretic, magnetophoretic, and chemotactic principles are being investigated in the biofabrication domain to direct patterning of cells within bioink constructs. This work describes a new acoustophoretic three-dimensional (3D) biofabrication approach that utilizes radiation forces generated by superimposing ultrasonic bulk acoustic waves (BAW) to preferentially organize cellular arrays within single and multi-layered hydrogel constructs. Using multiphysics modeling and experimental design, we have characterized the effects of process parameters including ultrasound frequency (0.71, 1, 1.5, 2 MHz), signal voltage amplitude (100, 200 mVpp), bioink viscosity (5, 70 cP), and actuation duration (10, 20 min) on the alignment characteristics, viability and metabolic activity of human adipose-derived stem cells (hASC) suspended in alginate. Results show that the spacing between adjacent cellular arrays decreased with increasing frequency (p < 0.001), while the width of the arrays decreased with increasing frequency and amplitude (p < 0.05), and upon lowering the bioink viscosity (p < 0.01) or increasing actuation duration (p < 0.01). Corresponding to the computational results wherein estimated acoustic radiation forces demonstrated a linear relationship with amplitude and a non-linear relationship with frequency, the interaction of moderate frequencies at high amplitudes resulted in viscous perturbations, ultimately affecting the hASC viability (p < 0.01). For each combination of frequency and amplitude at the extremities of the tested range, the hASC metabolic activity did not change over 4 days, but the activity of the low frequency-high amplitude treatment was lower than that of

the high frequency-low amplitude treatment at day 4 (p < 0.01). In addition to this process-structure characterization, we have also demonstrated the 3D bioprinting of a multi-layered medial knee meniscus construct featuring physiologically-relevant circumferential organization of viable hASC. This work contributes to the advancement of scalable biomimetic tissue manufacturing science and technology.

#### 1. Introduction

Musculoskeletal soft tissues such as ligaments, tendons and knee menisci are characterized by unique organization of their cellular and extracellular constituents, which is central to their primary functions [1–4]. For example, the cells and collagen fibers of ligaments and tendons, which primarily experience uniaxial tensile loads, are generally well-aligned along the direction of tensile loading [5–7]. Likewise, the predominantly circumferential organization of collagen bundles and cells in the semilunar wedge-shaped menisci allows them to resist hoop stresses experienced in the knee joint [8,9]. Such structure-function relationships are also evident in other types of soft tissues including cardiac tissue [10,11], corneal stroma [12,13], liver tissue [14,15], vasculature [16,17], and intestines [18,19]. Unfortunately, soft tissue injuries are highly prevalent (e.g., over a million annual incidences of anterior cruciate ligament and meniscus injuries [20–22]), and current treatments including surgical repair, allo/autografts and metal-polymer implants have limitations [23–25]. Hence, investigation and development of engineered tissue alternatives has become important.

Biofabrication processes including bioprinting have gained prominence over the last decade because of their ability to incorporate living cells within the process of creating engineered tissue constructs [26-29]. A majority of current biofabrication processes enable us to reproduce the patient-specific macro-scale three-dimensional (3D) geometry. However, it is equally important for these processes to be able to recapitulate tissue-specific spatial organization of cells. Otherwise, the homogenous distribution of cells throughout the bulk constructs would subsequently lead to an unorganized cell-secreted extracellular matrix (ECM) network as the constructs mature. Towards this, scaffold-based approaches typically rely on the contact guidance principle (i.e., topographical cues to direct cells). Alternatively, acoustophoretic [30,31], electrophoretic [32,33], photophoretic [34,35], magnetophoretic [36,37] and chemotactic [38,39] principles are being investigated to align cells into controlled spatial patterns within fluid matrices in the biofabrication domain. Among the aforementioned approaches, acoustophoretic processes are characterized by their non-contact (i.e., non-reliance on physical cues) and label-free (i.e., non-reliance on magnetic or chemical tags) cell manipulation modality. A number of acoustophoretic studies have utilized surface acoustic waves (SAW) for biomedical applications including cell sorting and separation [40,41], mixing [42], patterning [30,43] and transportation [43]. These SAW-based approaches are typically suitable for two-dimensional (2D) patterning and manipulation of single cells or multi-cell clusters in the microfluidics domain [44-46], but their acoustic radiation force fields are often inadequate for bulk 3D patterning in thicker viscous hydrogel matrices relevant for 3D biofabrication. Herein, bulk acoustic waves (BAW)-based approaches can be more relevant.

This paper describes a new ultrasonic BAW-based biofabrication approach to engineer 3D constructs featuring preferential alignment of cells relevant to native tissues. The fundamental process principle entails the manipulation of cells into controlled spatial patterns using acoustic

radiation force fields resulting from a longitudinal standing BAW in the bioink contained within an ultrasound-assisted biofabrication (UAB) chamber. By using appropriate ultrasonic actuation and bioink deposition and crosslinking parameters to generate acoustic radiation forces large enough to rapidly align and entrap cells while maintaining their viability, the process offers a synergistic mechanism for creating single and multi-layered 3D constructs with intrinsic cellular patterns. The open-top configuration of the UAB chamber, which is necessary to allow integration with 3D bioprinting to create multi-layered constructs with patient-specific geometry, further distinguishes our work from previous BAW-based approaches [47–49].

The primary goal of this work was to characterize the fundamental mechanics of the UAB process, including the critical process-structure relationships, in creating 3D constructs with highly organized cellular arrays using computational modeling and experimental design. Furthermore, the ultrasound-assisted bioprinting (UABp) of a multi-layered human knee meniscus construct featuring physiologically-relevant circumferential cellular patterns was also demonstrated. Alginate was used as the model hydrogel due to its wide usage in tissue engineering on account of its biocompatibility and immunoisolation characteristics [50,51]. Human adipose-derived stem cells (hASC) were used as the model cell line given their ability to differentiate into chondrocytes, fibroblasts, adipocytes and osteoblasts, which are constitutive of musculoskeletal tissues [52], and their use in meniscus tissue engineering and regenerative medicine literature [53–58].

## 2. Mechanics of aligning cells suspended in the bioink using ultrasound

Figure 1 shows a schematic of the platform central to UAB. In this platform, the pressure wave generated from a vibrating piezo-transducer in contact with the bioink interferes with the wave's reflection from an opposing reflecting surface, resulting in a longitudinal standing BAW in the bioink, prior to it being crosslinked. The voltage signal parsed to vibrate the transducer is sinusoidal with frequency in the ultrasonic range. The acoustic pressure along the x-axis (figure 1) of the BAW is given by equation (1) [59].

$$p(x,t) = P_o \cos(2\pi f t) \cos\left(\frac{2\pi f x}{c}\right) \tag{1}$$

where,  $P_o$  is the pressure amplitude in the bioink layer at the interface with the transducer, f is the transducer vibration frequency, and c is the longitudinal pressure wave speed in the bioink. An important hard wall boundary condition of zero fluid particle velocity (equation (2)) at the reflective surface (x = L) constrains the separation between the transducer and reflecting glass surface (L), necessary to generate a BAW, to an integer multiple of half the wavelength  $(\lambda)$  of ultrasound (equation (3)).

$$v(L,t) = -\frac{1}{\rho_b} \int_0^t \frac{\partial p}{\partial x} dt = 0$$
 (2)

$$L = \frac{nc}{2f} = \frac{n\lambda}{2} \tag{3}$$

where  $\rho_b$  is the density of bioink and n is the number of pressure nodes (p=0) in BAW, which appear as 2D planes parallel to the ultrasound-generating transducer surface and separated by half the wavelength. Each cell, assumed to be a near buoyant spherical particle, suspended between any two adjacent pressure nodes in the bioink experiences acoustic radiation force [60] (equation (4)), which pushes it towards the nearest pressure node.

$$F_{radiation} = \left(\frac{\pi}{24}\right) (k_b - k_c) d^3 \left(\frac{2\pi}{\lambda}\right) P_o^2 \sin\left(\frac{4\pi x}{\lambda}\right) \tag{4}$$

where d is the cell diameter, and  $k_b$  and  $k_c$  are the compressibility of the bioink (hydrogel solution) and cell, respectively. While the cell traverses to a pressure node, it experiences a fluid resistive force (Stokes drag [61] at low Reynolds number) from the bioink (equation (5)).

$$F_{resistive} = 3\pi \eta dv \tag{5}$$

where  $\eta$  is the dynamic viscosity, and v is the instantaneous velocity of the cell.

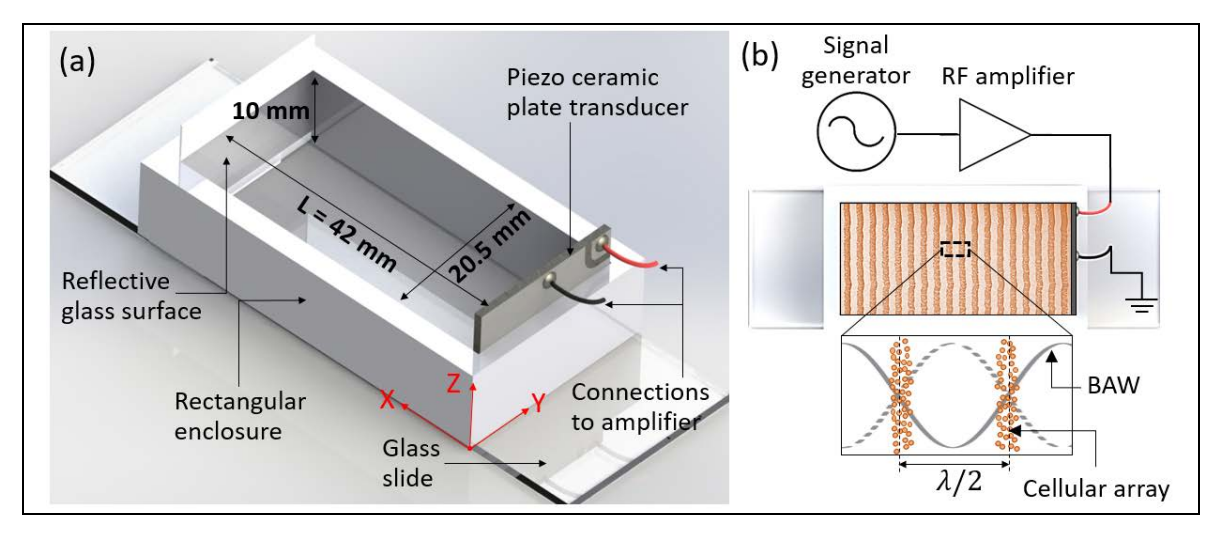


**Figure 1.** (a) Platform for ultrasound-assisted biofabrication (UAB) and bioprinting (UABp). (b) Schematic of acoustic field distribution with nodal and antinodal regions within longitudinal standing bulk acoustic wave (BAW). The cells cluster at the nearest nodal plane forming a cellular array.

Equations (1)-(5) can have several practical implications. First, increasing the ultrasound frequency would result in smaller separation between the pressure nodes and resulting cell clusters (arrays) at the nodes. Second,  $F_{radiation}$  exceeding  $F_{resistive}$  would facilitate movement of cells to the nodes. As such,  $F_{resistive}$  will be higher in bioinks with higher viscosities. In this scenario, the correspondingly higher  $F_{radiation}$  can be achieved by increasing the pressure amplitude. Finally, increasing the duration of transducer actuation would provide more time for the cells to migrate to the nodes [62], thereby creating more closely packed cellular arrays.

## 3. Materials and Methods

An overview of the computational modeling (Study 1) and experimental characterization (Studies 2-5) is presented in figure 2. First, a multiphysics finite element (FE) model was created to determine the longitudinal BAW pressure distribution characteristics that govern the alignment of suspended cells. This formed the basis of Study 2 wherein the effects of ultrasound frequency (0.71 MHz, 1 MHz, 1.5 MHz, and 2 MHz) and signal source voltage amplitude (100 mV<sub>pp</sub> and 200 mV<sub>pp</sub>) on the alignment characteristics (spacing between adjacent arrays of aligned cells and the degree of cell concentration at pressure nodes) of hASC suspended in alginate solution was experimentally characterized. In Study 3, the effects of the two extreme frequencies (0.71 MHz and 2 MHz) and the two amplitudes on the metabolic activity of aligned hASC in crosslinked alginate constructs over 4 days were investigated. In Study 4, the effects of alginate viscosity (5

cP and 70 cP) and actuation duration (10 min and 20 min) on hASC viability and alignment characteristics were assessed. Finally, in Study 5, the computational modeling and UABp of multi-layered alginate constructs with circumferential hASC alignment patterns was demonstrated.

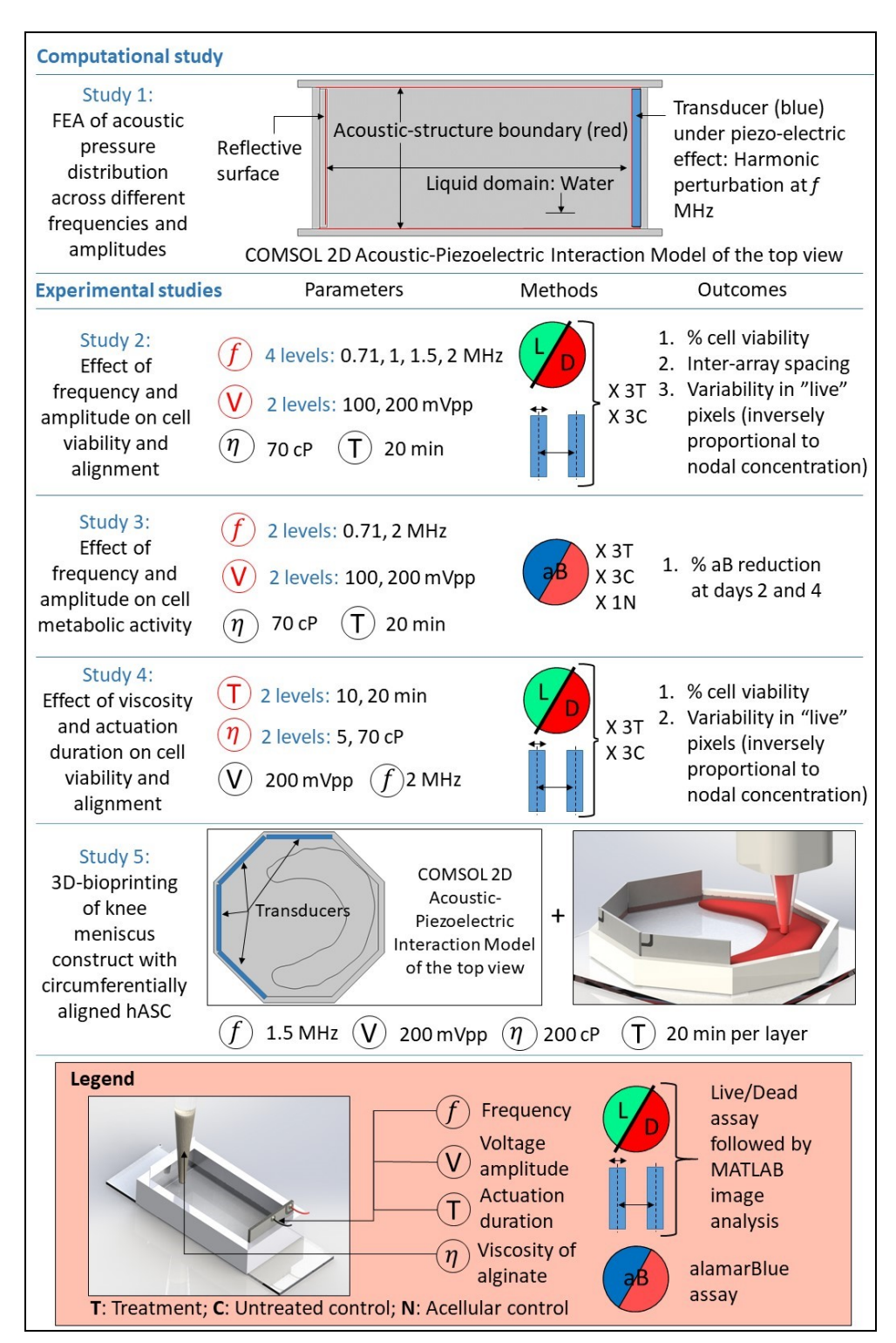


**Figure 2.** Overview of the computational and experimental studies. All parameters within each experimental study are fully crossed.

## 3.1. UAB platform design and fabrication

The UAB platform is comprised of two primary units – bioink chamber and power-signal source (figure 1). The bioink chamber design is primarily informed by equation (3), wherein the separation between the BAW-inducing transducer and reflective surfaces (L) should be an integer multiple of half the wavelength. For each of the four frequencies (table 1), L = 42 mm satisfies this requirement. To achieve lowest transducer impedance and maximum compliance (straining due to applied voltage), different transducers were procured pertaining to different resonant frequencies. Accounting for the transducer thickness that is a characteristic of its resonant frequency and reflective cover glass thickness (0.2 mm), the chamber was custom-designed for each frequency to achieve an effective L of 42 mm and width and thickness of 20.5 mm and 10 mm, respectively. The rectangular enclosures were 3D printed out of acrylonitrile butadiene styrene (ABS) (uPrint SE Plus, Stratasys, Eden Prairie, MN) and covered with Tegaderm™ film (3M Technologies, St. Paul, MN) to render the surfaces biocompatible and electrically insulating. Next, a Corning® cover glass (Sigma-Aldrich, St. Paul, MN) and appropriate piezo ceramic plate transducer (Steiner and Martins Inc., Dorsal, FL) covered with Tegaderm film were attached to opposing ends of the ABS enclosure. Finally, the upfitted enclosure was affixed onto a Corning microscope slide (Sigma-Aldrich) on the bottom to complete the bioink chamber construction. Each chamber was tested to ensure there was no leakage of liquid or current. At the beginning of each experiment, the transducer terminals were connected to a function generator (Keysight Technologies Inc. Santa Rosa, CA) via an intermediate high frequency radio frequency power amplifier (240L, 10 kHz – 12 MHz bandwidth, Electronics & Innovation Ltd., Rochester, NY).

**Table 1.** Transducer resonant frequencies and corresponding theoretical spacing between adjacent BAW pressure nodes and expected number of such nodes (assuming c = 1500 m/s).

f	0.71 MHz	1 MHz	1.5 MHz	2 MHz
λ/2	1.05 mm	0.75 mm	0.5 mm	0.375 mm
n	40	56	84	112

#### 3.2. Computational modeling of BAW pressure distribution

Under ideal theoretical conditions (section 2), BAW nodes appear along planes parallel to the actuated transducer and reflective surfaces. Herein, the effects of potential wave reflection from the chamber sidewalls is neglected, and strain across the surface of the transducer in response to the sinusoidal voltage signal is assumed to be uniform. However, these assumptions do not hold in practice. Therefore, built upon the foundational analysis by Scholz et al [63], we have developed a 2D linear acoustic FE model in COMSOL Multiphysics® (Comsol Inc., Burlington, MA) accounting for transducer compliance and loss parameters and attenuation within the fluid domain to more accurately map the BAW pressure distribution in the bioink chamber of the UAB platform. To set up the model (figure 2, top panel), first, the 2D acoustic-piezoelectric interaction (frequency domain) model consisting of the pressure acoustics, structural mechanics and electrostatics physics interfaces was selected. Then, given that the primary component of alginate solutions is water (98%), water with frequency dependent attenuation per unit length as per existing empirical data [64] was assigned to the acoustics interface as the liquid domain between

the piezo-transducer and glass reflective surface. A modified PZT-4 (density 7900 kg/m<sup>3</sup>) was the piezoelectric domain assigned to the structural mechanics and electrostatics interface. The enclosure (ABS) was assigned to the structural mechanics interface. Within the structural mechanics interface, stress-charge form of equations and manufacturer's specifications [65] were used to define the transducer compliance – elastic matrix coefficients ( $c_{E(11)}$  = 86 GPa and  $c_{E(33)}$  = 73 GPa), piezoelectric constants ( $e^{T}_{(31)} = -12.4 \text{ C/m}^2$  and  $e^{T}_{(33)} = 23.36 \text{ C/m}^2$ ), and structural and dielectric loss factors (1/1800 and 0.4, respectively). A fixed constraint was then assigned to all edges of the chamber enclosure other than the transducer edge that interfaces with the liquid. To this edge, in the electrostatics interface, accounting for the 50 dB amplification of input voltage in the experimental studies, a harmonic actuation with amplitude of 16 V or 32 V corresponding to 100 mVpp or 200 mVpp input voltage, respectively, was applied. Following these steps, an acoustic structure boundary was automatically defined at all edges where liquid is in contact with solid, and piezoelectric effect was defined at the transducer. A free triangular mesh was defined for all domains with maximum element size of 30 µm to fulfil the convergence criterion of mesh size less than  $\lambda/10$  for each frequency [63]. At each frequency, the transducer thickness was modeled as per manufacturer's specification. The model was computed (top view) at the four frequencies and two voltage amplitudes corresponding to the experimental design to estimate the BAW pressure distribution and peak acoustic pressures generated within the bioink chamber.

## 3.3. Experimental Assessment of Transducer Pressure Fields

In order to experimentally validate the relationship between input voltage amplitude and resulting peak acoustic pressure, pressure fields across the wave-generating surfaces of transducers were assessed using a hydrophone (HGL0200, Onda Corp., Sunnyvale, CA). Transducers of all four frequencies were tested at both input voltage amplitudes. Briefly, a custom-designed setup was 3D printed (ABS) in order to position the sensing surface of the hydrophone parallel to and 30 mm apart from the transducer's wave-generating surface (figure S1). The 30 mm separation represented the distance between transducer and center of the constructs inside the bioink chamber during the biofabrication experiments. To measure the pressure field, the transducer was actuated as the hydrophone traversed the y-z plane in steps of 0.025 mm and scan time of 100 ms at each step using a custom linear stage control interface in LabView (National Instruments, Austin, TX). Using a calibrated custom MATLAB (MathWorks, Natick, MA) program, the maximum voltage at the output of the hydrophone at each step was transformed into acoustic pressure amplitude. Thus, the entire y-z plane scan resulted in a map of the pressure field across the wave-generating surface of the transducer.

#### 3.4. Alginate-hASC bioink preparation

Passage 1 hASC (StemPro<sup>™</sup> R7788115, Thermo Fisher Scientific, Waltham, MA) were used in all studies. Cryopreserved cells were thawed and cultured (37°C, 5% CO<sub>2</sub>) in T-75 flasks (Nunc<sup>™</sup> Easy Flask<sup>™</sup>, Thermo Fisher Scientific) with MesenPRO RS<sup>™</sup> basal medium with growth supplement (Thermo Fisher Scientific) and 1% L-Glutamine (Thermo Fisher Scientific) at a seeding density of 250,000 cells per flask. Media changes were performed every 48 h until 80% confluency was reached.

A higher viscosity sodium alginate (Manugel® GMB, DuPont, Wilmington, DE) was used as the bioink matrix in all four experimental studies. Additionally, a lower viscosity sodium alginate

(Protanal® LFR 5/60, DuPont) was used in Study 4. For each study, for one or both types of alginates as necessitated by the experimental design, 30 ml of 2% w/v hydrogel solution was prepared by mixing the appropriate proportions of alginate powder in sterile phosphate buffered saline (PBS) (Sigma-Aldrich) in a 50 ml tube and vortexing for 1 min followed by sonication at 60 Hz for 1 h. The solution was then incubated (37°C) for 72 h to make it more homogenous. Finally, the solution was autoclaved at 121°C and 16 psi for 30 min (BioClave 16, Benchmark Scientific Inc, Sayreville, NJ) for terminal sterilization. Relevant to Study 4, the average dynamic viscosity of the higher and lower viscosity autoclaved solutions were determined to be 70 cP and 5 cP, respectively, using a rheometer (Brookfield, Middleborough, MA).

To concoct the bioink, the hASC were harvested from 80% confluent flasks by washing with 4 ml of Hank's balanced salt solution (Sigma-Aldrich) followed by addition of 2 ml of 0.25% Trypsin-EDTA (Sigma-Aldrich). The trypsinized cell suspension was neutralized with 4 mL of media after 5 min and centrifuged at 120 g for 5 min to obtain the cell pellet. The pellet was gently mixed with the appropriate volume of sterilized 2% alginate solution to obtain the bioink with a concentration of  $1\times10^6$  cells/ml.

## 3.5. UAB of alginate constructs with aligned hASC

This section describes the fundamental protocol used to create alginate constructs with aligned cellular arrays using the UAB platform (figure 3). The process parameters (frequency, amplitude, alginate viscosity, actuation duration) utilized in each experiment using this protocol were governed by the study design (figure 2).

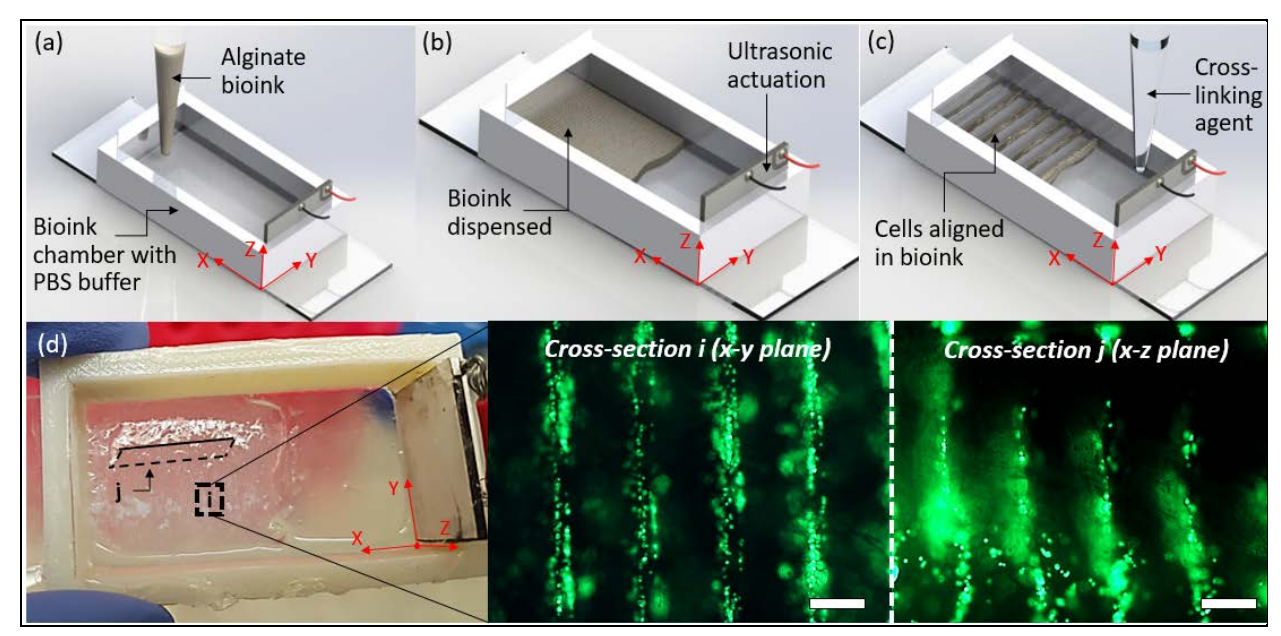


**Figure 3.** Biofabrication of alginate constructs with ultrasonically aligned cells. (a) Alginate bioink with homogeneously suspended cells  $(1\times10^6 \text{ cells/ml})$  is deposited into the bioink chamber containing PBS buffer. (b) Transducer is actuated in thickness mode. (c) Bioink is chemically crosslinked as the cells align along nodal planes parallel to transducer surface. (d) A representative construct (2 MHz bioink chamber) with aligned hASC as seen from the top (x-y plane) and at a cross-section depicting alignment along the thickness of the construct (x-z plane). Scale bar = 250  $\mu$ m.

Prior to each experiment, the bioink chamber was disinfected by repeated swabbing with 70% ethanol followed by 30 min exposure to UV radiation inside a biosafety cabinet. The transducer was then connected to the voltage source via the power amplifier. To begin fabrication of the construct, 4 ml of PBS was added to the chamber, and the appropriate actuation signal was applied in 1 s bursts with a 1.5 s pause. Next, 1 ml of the bioink with a concentration of 1×106 cells/ml was deposited into the actuated chamber. Actuating the transducers in burst mode as opposed to continuous mode allowed to reduce Stokes drag on cells and prevent overheating and loss in compliance properties of the transducer. After 1 min, 4 ml of 0.5% w/v sterile CaCl<sub>2</sub> was introduced at the rate of 2 ml/min to initiate alginate crosslinking. The actuation signal was turned off after the intended duration as per the study (figure 2). The construct was further crosslinked in 1% and then 2% sterile CaCl<sub>2</sub> solution for 20 min each. This serial gelation protocol was established in our lab prior to commencing the experimental design in order to obtain reproducible high-fidelity constructs that are minimally affected by the ion exchange that occurs during crosslinking. Finally, the gelled construct (thickness = 3.5 ± 0.5 mm) was aseptically transferred from the chamber to a six-well plate pre-filled with 3 ml of media, and incubated for 3 h at 37°C and 5% CO<sub>2</sub>, before being utilized for further analyses.

## 3.6. UABp of alginate knee meniscus construct with circumferentially-aligned hASC

Based on the fundamental principles of UAB (section 2), an octagonal bioink chamber comprising of four pairs of 1.5 MHz transducers and opposing reflecting surfaces, with L = 75 mm, was designed and fabricated following previously described procedures (section 3.1). Size of the chamber was governed by the size of the biomodeled medial knee meniscus [55]. To computationally estimate the peak acoustic pressure within the bioink and expected BAW pressure distribution pattern prior to experimentation, a COMSOL model of the octagonal chamber (top view) was created using the previously described procedure (section 3.2). The transducers were actuated one at a time to mimic the experimental procedure described below to achieve requisite circumferential alignment. For Study 5 experiments, the octagonal chamber was integrated with a commercial extrusion-based 3D bioprinter (BioAssemblyBot<sup>™</sup>, Advanced Solutions Life Sciences, Louisville, KY). Alginate (Manugel® GMB) disinfected by 1 h exposure to UV radiation was used as the bioink matrix for this study. The viscosity of this UV-disinfected solution (200 cP) makes it more suitable for multi-layered 3D bioprinting than the autoclaved solution (70 cP). Neutral red-stained (N 2889, Sigma-Aldrich) hASC suspended within this alginate (1×106 cells/ml) constituted the bioink. The STL file of the medial knee meniscus, sliced with a layer height of 1.2 mm, was setup in the TSIM® software (Advanced Solutions Life Sciences) to ensure that the subsequent bioprinting occurred within the octagonal chamber. A total of 7 ml of bioink was bioprinted with an extrusion pressure of 15×10<sup>-3</sup> N/mm<sup>2</sup> at 37 °C through a 25G nozzle at a speed of 12 mm/s in a total of 4 layers to create the 3D meniscus construct. Throughout the bioprinting cycle, circumferential alignment was imparted to cells within each layer through serial actuation of the 1.5 MHz transducers at 200 mVpp via high-frequency relays (G6K 2P RF, Omron Electronics LLC, IL). One-at-a-time actuation (1 s actuation before switching to adjacent transducer) alleviated the need for burst mode signal and prevented interference of the pressure waves that would otherwise simultaneously emanate from the other transducers to disrupt the cell alignment. A gelation protocol similar to the one described in section 3.5, with the

crosslinker (CaCl<sub>2</sub>) added between layers, was used to entrap the cells within the constructs as they were being aligned.

#### 3.7. Assessment of constructs fabricated via UAB and UABp

Cell viability, spacing between centroids of adjacent arrays of viable cells (henceforth referred to as inter-array spacing), and the degree of concentration of viable cells at the nodes (henceforth referred to as nodal concentration) were the three outcome metrics of interest for Studies 2 and 4. Cell metabolic activity was the primary metric for Study 3.

The LIVE/DEAD® assay (Life Technologies, Carlsbad, CA) was used to assess hASC viability in the crosslinked constructs. The sample size was n = 3 constructs for each of the treatment (UAB) and control (bioink not subject to UAB) groups. After 3 h of incubation post-fabrication, 1 ml of PBS containing 0.5 µl calcein AM and 2 µl EthD-l was added to the constructs followed by 15 min of further incubation. Subsequently, each construct was imaged at three random locations using a fluorescence microscope (DM5500B, Leica Microsystems, Wetzlar, Germany). The live/dead images were analyzed using a custom MATLAB script to determine % cell viability (N = 9 images per experimental and control group). Briefly, a maximal gradient method for edge detection was applied to sharpened grayscale translations of red and green fluorescent images, followed by Hough transformation to detect circles within a range of diameters relevant for hASC, and % cell viability computed from these estimates of live and dead cells.

To measure the inter-array spacing and the nodal concentration, the live/dead images of all experimental groups were analyzed using another custom MATLAB script (N = 18 images per group). Briefly, an edge detection protocol was applied to detect "live" pixels corresponding to viable cells within a user-specified bounding box (n = 2 per image) enclosing two adjacent aligned cellular arrays. The separation between the centroids of adjacent arrays of aligned cells signified the inter-array spacing. The standard deviation of positions of "live" pixels derived from their distribution about their array's centroid along the x-axis was a measure of the nodal concentration (signifying width of cell arrays), with lower standard deviations indicating higher nodal concentrations. All image analysis scripts are provided as supplemental information.

The alamarBlue® (aB) assay (Thermo Fisher Scientific) was used to assess the hASC metabolic activity over 4 days. The sample size was n = 3 constructs for each of the treatment and untreated control groups. An additional acellular control was included in each experiment to normalize the aB readings. Each crosslinked construct was cultured in 4 ml of media in a six-well plate (37°C, 5% CO<sub>2</sub>), with media changes performed every 24 h. At days 2 and 4, the supernatant media was replaced with 4 ml of fresh media containing 10% v/v of the aB reagent. After 4 h, three 1 ml media samples from each construct were analyzed for absorbance on a micro-plate reader (Tecan, Männedorf, Switzerland) at 570 nm and 600 nm excitation and emission wavelengths, respectively. The absorbance data normalized to the acellular control is reported as % aB reduction. In addition, to verify persistence of the ultrasound-induced cellular alignment over 4 days in culture, separate constructs of the 2 MHz – 100 mVpp and 2 MHz – 200 mVpp groups were analyzed via live/dead assay and MATLAB image analysis.

In Study 5, top-down images of the meniscus construct were captured at different zones along its semilunar contour and at a vertical cross-section using a dissection microscope (EZ4 D, Leica Microsystems) and a fluorescence microscope (Leica DM5500B) to ascertain the circumferential alignment of viable cells.

#### 3.8. Statistical analyses

For Studies 2-4, two-way ANOVA and Tukey post-hoc tests were used to assess the effects of the corresponding two independent factors and their interactions on the appropriate metrics of interest. Additionally, for Studies 2 and 3, t-tests were performed to compare % cell viability and % aB reduction, respectively, between experimental and control groups. The normality and homoscedasticity of all data was assessed using Shapiro-Wilk W test and Brown-Forsythe test, respectively. All tests were performed in JMP® (SAS, Cary, NC) and statistical significance assessed at  $\alpha$  = 0.05.

#### 4. Results

#### 4.1. Study 1: FE model of longitudinal BAW pressure distribution

A top view of the COMSOL output demonstrating the absolute acoustic pressure distributions in the bioink chamber at different frequencies is shown in figure 4a. Analogous to theory, the BAW pattern consisted of nodal planes parallel to the transducer surface. The scalloped profiles of the nodal planes can be attributed to the COMSOL model accounting for the manufacturer-specified transducer compliance and loss parameters and wave reflections from side walls of the chamber. The number of FE-estimated nodal planes matched the theoretical estimates (table 1), and an increase in frequency resulted in a decrease in the width of the nodal planes as well as a decrease in the spacing between adjacent nodal planes.

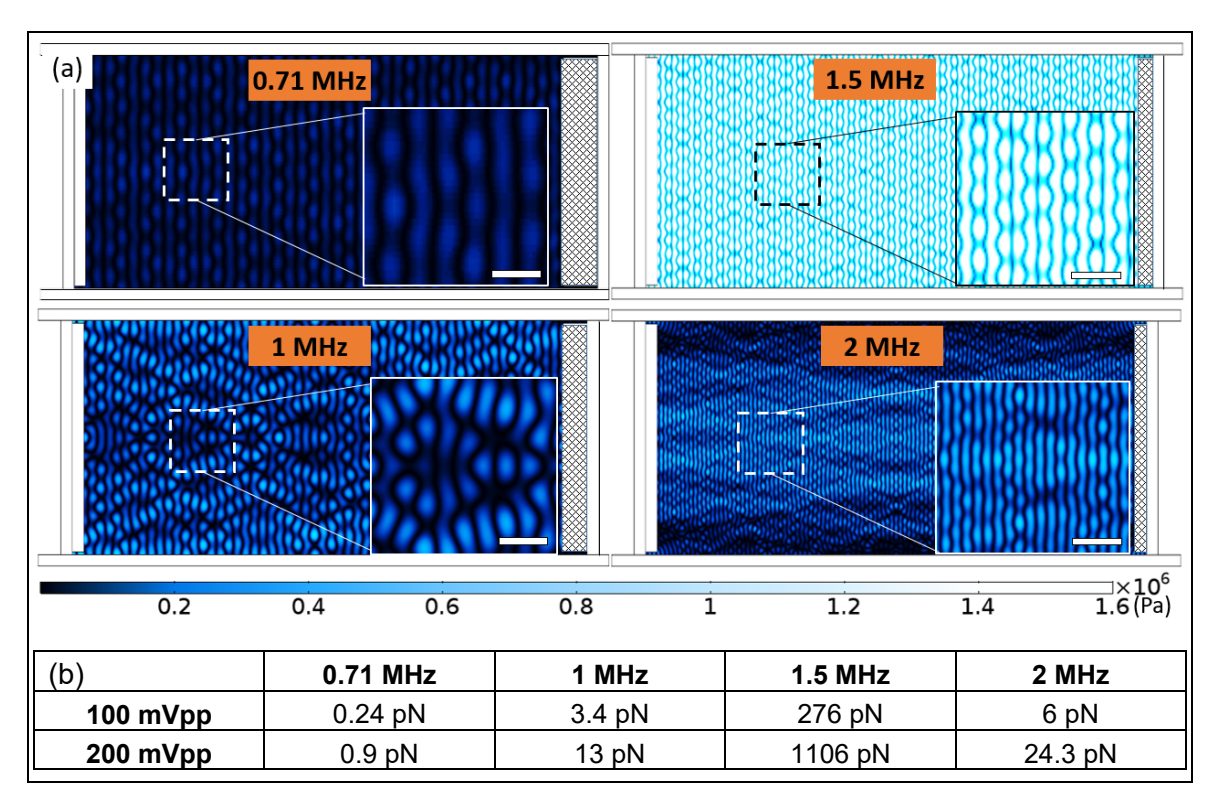


**Figure 4.** (a) Top view of the absolute acoustic pressure distribution across the UAB bioink chamber (and magnified insets; scale bar = 2 mm) at 200 mVpp voltage amplitude across different frequencies. Thickness of transducers (indicated by cross-hatched pattern on the right in each figure) is dependent on the resonant frequency. (b) Estimates of  $F_{radiation}$  experienced by cells at different frequencies and amplitudes.

The peak acoustic pressure had a direct relationship with the input voltage amplitude. Doubling the voltage amplitude doubled the computationally-estimated peak pressure, and this relationship was corroborated by the hydrophone data (figure 5a). This, in turn, would have resulted in quadrupling of the radiation force acting on the cells (equation (4)). Furthermore, the relationship between transducer frequency and peak pressure was determined to be non-linear, both computationally and experimentally, with maximum peak pressure achieved at 1.5 MHz and minimum at 0.71 MHz. The theoretical estimates of  $F_{radiation}$  experienced by cells at different frequency and voltage amplitude combinations, computed from the FE-estimated peak pressures for hASC ( $d = 21 \,\mu\text{m}$ ,  $k_c = 40 \times 10^{-11} \,\text{Pa}^{-1}$ ) in water ( $k_b = 45.8 \times 10^{-11} \,\text{Pa}^{-1}$ ), are presented in figure 4b. Higher voltage amplitude resulted in higher  $F_{radiation}$  across all frequencies, and the highest  $F_{radiation}$  was noted at 1.5 MHz for each voltage amplitude, following the similar non-linear relationship with frequency as acoustic pressure.

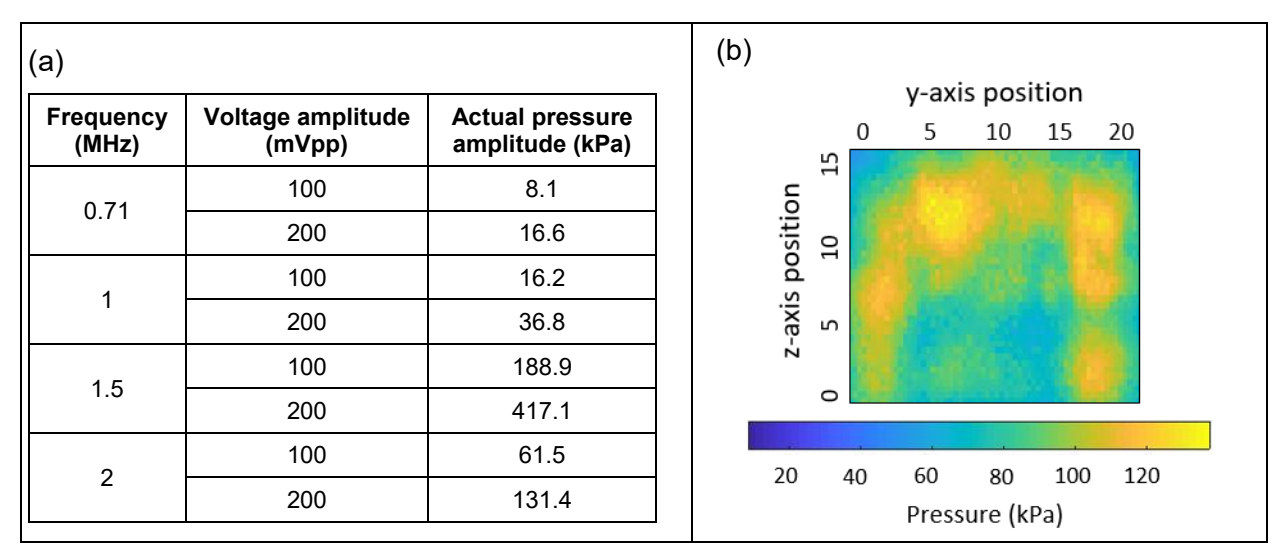


**Figure 5.** Experimental mapping of transducer pressure amplitude characteristics. (a) Peak pressure amplitudes at different combinations of frequency and input voltage amplitude. Similar to the computational model outcomes, doubling the voltage amplitude doubled the peak pressure at each frequency. Furthermore, the relationship between pressure and frequency was also found to be non-linear, with the highest pressure reported at 1.5 MHz, followed by 2, 1 and 0.71 MHz. (b) Representative image (2 MHz – 100 mVpp) of the non-uniform pressure field across the wave-generating surface of the transducer.

# 4.2. Study 2: Effects of frequency and voltage amplitude on hASC viability and alignment characteristics

Representative live/dead images at different frequency-amplitude combinations and summary of the % cell viability data from the experimental design are presented in figure 6. All Study 2 data satisfied normality and homoscedasticity assumptions. Results of the two-way ANOVA indicate that the interaction of frequency and amplitude had a significant effect on the viability of hASC (p = 0.002). The hASC viability of 1 MHz-200 mVpp group ( $56 \pm 12.7\%$ ) and the 1.5 MHz-200 mVpp group ( $58.4 \pm 4.3\%$ ) was significantly lower in comparison to every other treatment group as well as their corresponding untreated controls (p = 0.03 and 0.003, respectively). Of the other treatment groups, the hASC viability in only the 0.71 MHz-200 mVpp group ( $82 \pm 3.9\%$ ) was significantly lower than its corresponding untreated control ( $91.7 \pm 2.6\%$ ) (p = 0.035).

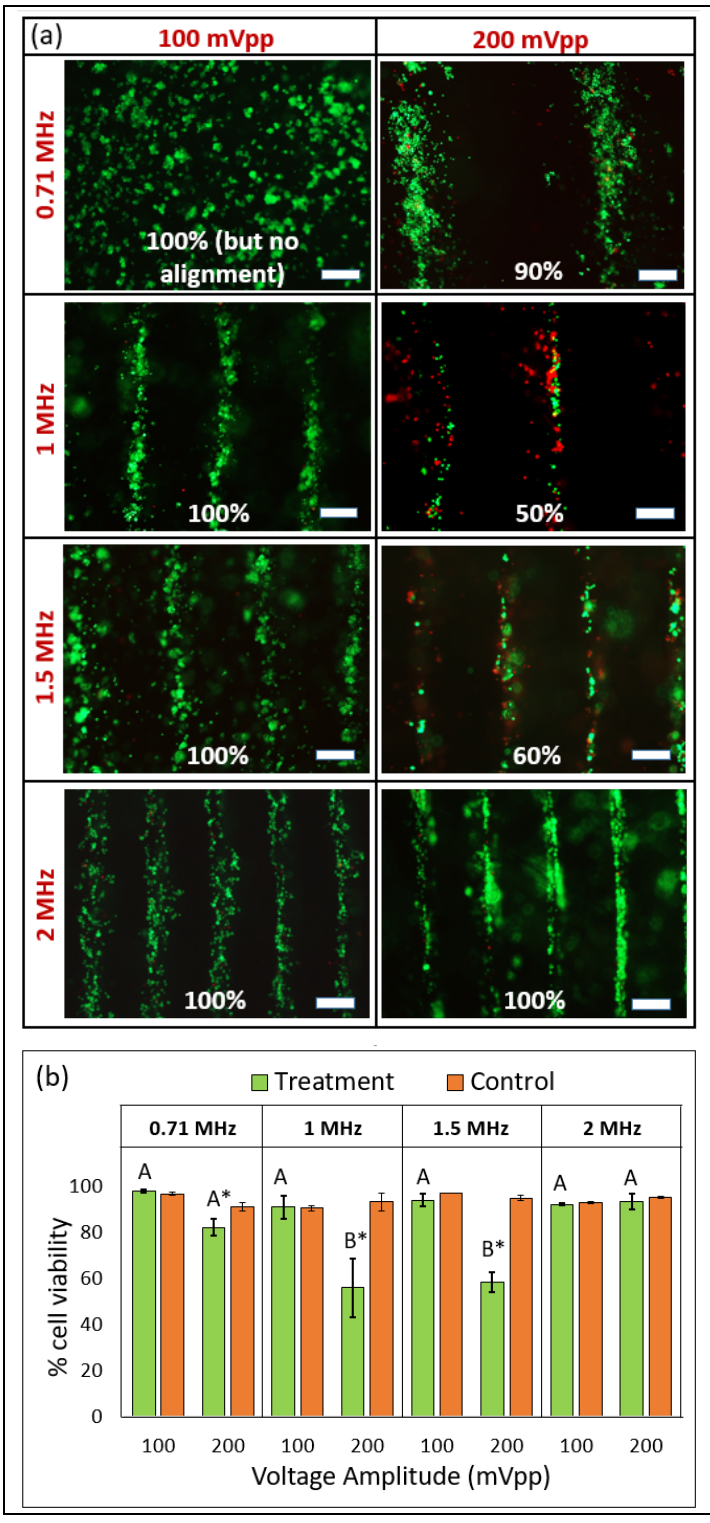


**Figure 6.** (a) Representative live/dead images of hASC-alginate constructs for all treatment and control groups with approximate % cell viability listed. Live/dead assay was performed 3 h post-fabrication. Scale bar =  $250 \mu m$ . (b) Summary of % cell viability data. Groups denoted by A and B were significantly different from each other (p < 0.05). ANOVA indicates a significant interaction effect of frequency and amplitude. \* indicates significant reduction in cell viability between corresponding treatment and control groups (p < 0.05).

The lower viability in the 1.5 MHz-200 mVpp group can be attributed to the elevated acoustic radiation force experienced by the cells. The estimated  $F_{radiation}$  for this group (1106 pN) was at least an order of magnitude higher than other groups (figure 4b). Among all treatment groups, the 1 MHz-200 mVpp and 0.71 MHz-200 mVpp groups exhibited the highest magnitude of perturbations during the experiments, resulting from turbulent streams induced due to non-uniform pressure field across the wave-generating transducer surface in practice (figures 5b and S2). But, the estimated  $F_{radiation}$  in the 1 MHz-200 mVpp group (13 pN) was more than a magnitude higher than that in the 0.71 MHz-200 mVpp group (0.9 pN). The combination of the perturbations and high acoustic radiation force can be postulated to have affected the hASC viability of that group.

The inter-array spacing for all treatment groups in the experimental design is summarized in figure 7. The theoretical values of the spacing ( $\lambda/2$ ; table 1) are also included in the plot. Of the eight treatment groups, 0.71 MHz-100 mVpp was the only group in which no alignment was observed. This can be attributed to low acoustic radiation force at this factor combination; the estimated  $F_{radiation}$  for this group (0.24 pN) was the lowest in the experimental design, up to three orders of magnitude smaller than that in the 1.5 MHz-200 mVpp group (1106 pN). The largest spacing was observed in the 0.71 MHz-100 mVpp group (1137.1 ± 65.4 µm) and smallest in the 2 MHz-200 mVpp groups (459.1 ± 37 µm). ANOVA results show that frequency had a significant effect on the inter-array spacing (p < 0.001), but the amplitude or their interaction did not. As such, the mean inter-array spacing for each treatment group was very close to its corresponding theoretical estimate. These findings corroborate the theory.

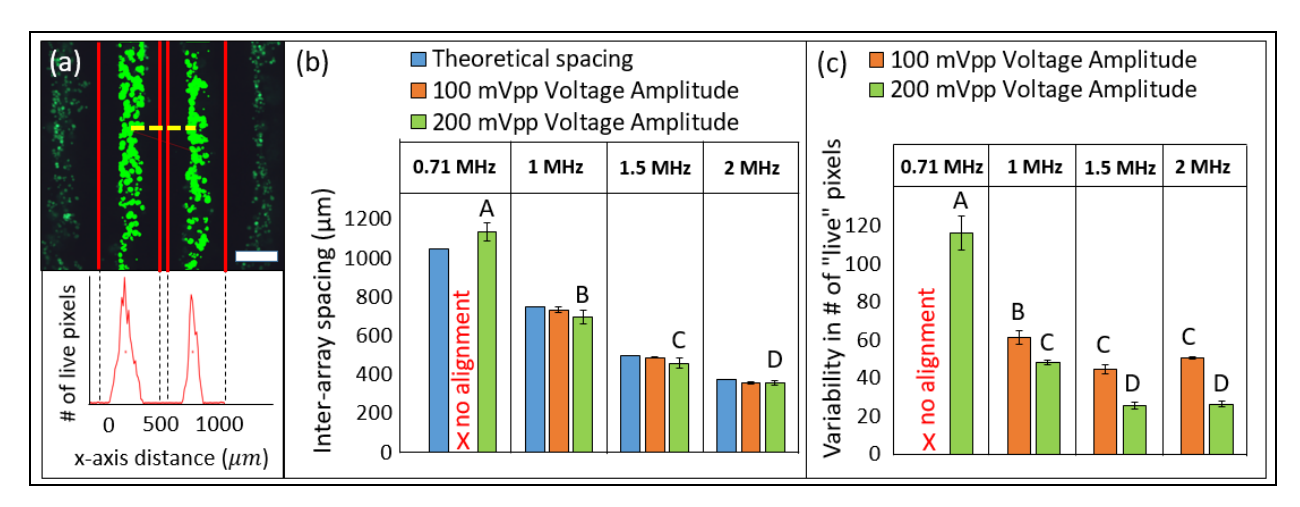


**Figure 7.** (a) Representative images highlighting the measurement of inter-array spacing and nodal concentration using MATLAB analyses. Scale bar =  $250 \mu m$ . (b) and (c) Summary of inter-array spacing and nodal concentration data, respectively. Groups denoted by A, B, C, and D were significantly different from each other (p < 0.05). Frequency had a significant effect on the inter-array spacing while the interaction of frequency and amplitude had a significant effect on the nodal concentration.

The nodal concentration data in terms of the variability in "live" pixels is summarized in figure 7c. The lowest variability in "live" pixels, corresponding to the highest nodal concentration, was observed in the 2 MHz-200 mVpp group (26.3  $\pm$  2.1) and the highest variability in the 0.71 MHz-200 mVpp group (116.6  $\pm$  12.6). ANOVA results show that the interaction effect of frequency

and amplitude was significant (p = 0.019). This indicates that at higher amplitudes and frequencies, the cells were more closely clustered along the nodal plane. Post-hoc tests indicate that the nodal concentrations for the 1.5 MHz-200 mVpp and 2 MHz-200 mVpp groups (variability in "live" pixels =  $25.3 \pm 2.6$  and  $26.4 \pm 2.1$ , respectively) were significantly higher than those of other groups (p < 0.05). Furthermore, the cells retained their alignment in cross-linked constructs over 4 days in culture for the two 2 MHz groups (figure S3). Despite these two groups being more susceptible to potential alignment disruption on account of possessing the smallest inter-array spacing post-fabrication, the constant nutrient exchange or potential turbulence during media replenishment did not affect the alignment.

## 4.3. Study 3: Effects of frequency and amplitude on metabolic activity of aligned hASC

The % aB reduction data from the experimental design is summarized in figure 8. All Study 3 data satisfied normality and homoscedasticity assumptions. The 0.71 MHz-100 mVpp group was excluded from the analysis due to the lack of cell alignment as reported earlier. For the two-way ANOVA, the frequency-amplitude combination was included as one factor and time point as the other. Results show that the interaction effect of frequency-amplitude and time point on hASC metabolic activity was significant (p = 0.003).

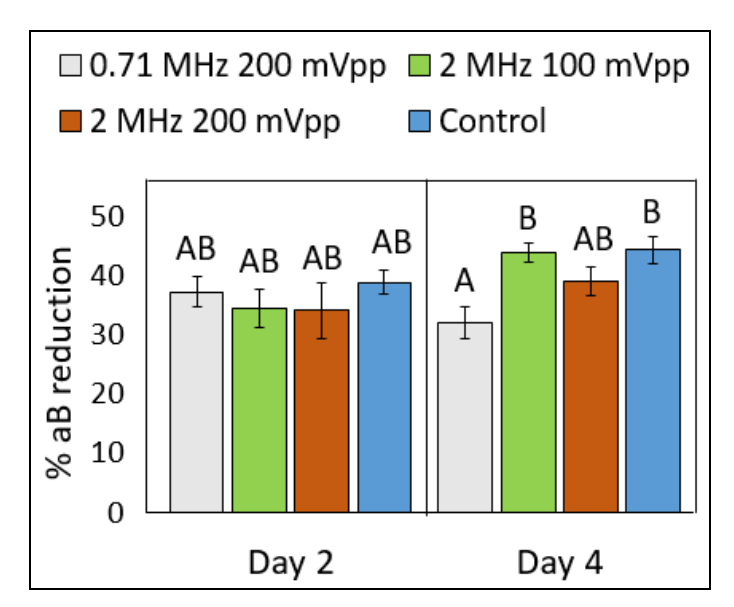


**Figure 8.** Results of hASC metabolic activity in constructs fabricated at different frequency-amplitude combinations over 4 days in comparison to untreated control groups. The groups denoted by A and B were significantly different from each other (p < 0.05). The groups denoted by AB were not different from either A or B groups. The interaction effect of frequency-amplitude combination and time point was significant. 0.71 MHz-100 mVpp combination was not included in the analysis since no alignment was observed.

Whereas the hASC viability in the 0.71 MHz-200 mVpp group was lower than its untreated control immediately after fabrication (figure 6b), the difference between their cell metabolic activities at day 2 was not significant. As such, at day 2, there was no statistically significant difference in the hASC metabolic activity between any of the four groups. Moreover, for each group, the change in metabolic activity from day 2 to 4 was also not significant. The only significant

difference observed in this experimental design was between the 0.71 MHz-200 mVpp group and the 2 MHz-100 mVpp and control groups at day 4 (p = 0.004 and 0.003, respectively).

# 4.4. Study 4: Effects of bioink viscosity and actuation duration on hASC viability and alignment characteristics

Previously, during Study 2, the bioink viscosity and actuation duration were held constant while assessing the effects of frequency and amplitude. For this study, all constructs were fabricated at 2 MHz and 200 mVpp while the bioink viscosity and actuation time were varied as per the experimental design. Figure 9 depicts representative live/dead images of constructs of different treatment groups and a plot summarizing the nodal concentration data. The viability was 100% across all groups, indicating that actuating 2 MHz transducers with 200 mVpp for up to 20 min did not adversely affect the viability of aligned hASC in crosslinked bioinks of viscosities up to 70 cP. The nodal concentration data satisfied normality and homoscedasticity assumptions, and ANOVA results show that the main effects of viscosity and actuation duration on the nodal concentration were significant (p = 0.003 for both). Among the four treatment groups, the cells were most tightly clustered along the nodal planes in the low viscosity bioink after 20 min of actuation (variability in "live" pixels =  $34.6 \pm 2.1$ ). At the other extreme, the width of the hASC arrays was the largest in the high viscosity bioink with shorter actuation duration (variability in "live" pixels =  $76.2 \pm 3$ ).

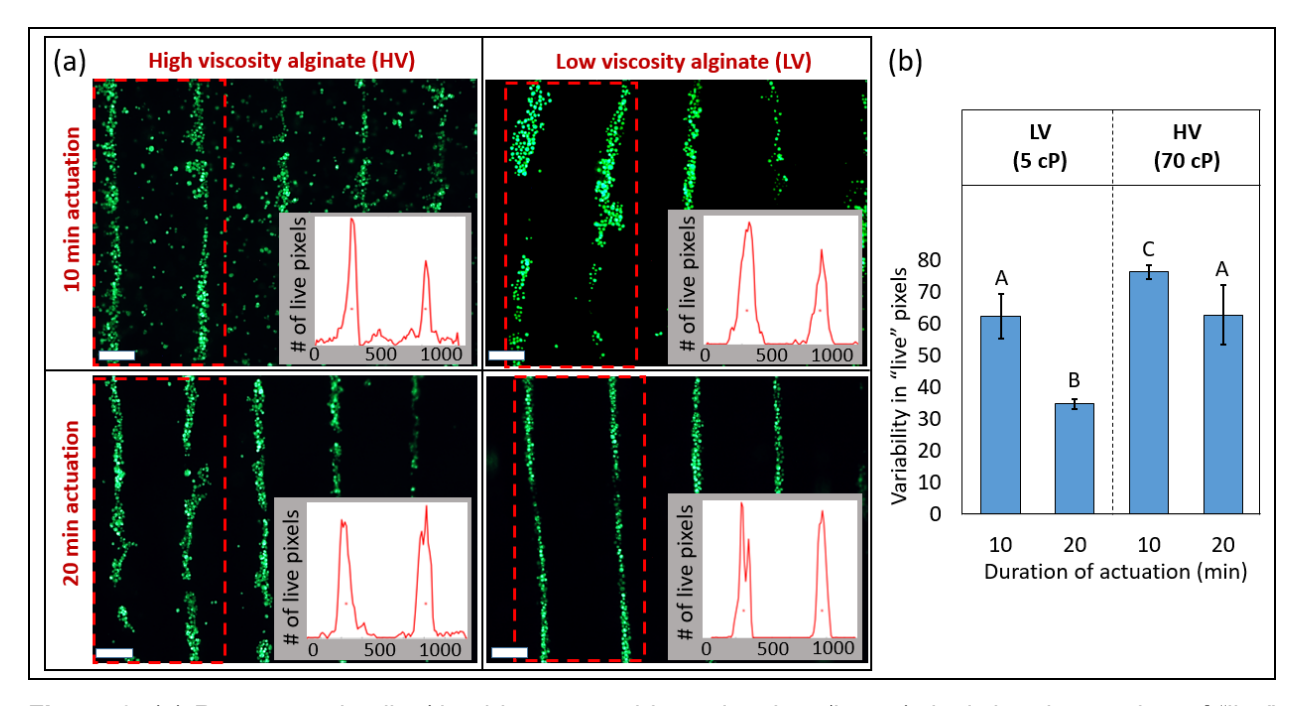


**Figure 9.** (a) Representative live/dead images and intensity plots (insets) depicting the number of "live" pixels along 1 mm of the x-axis within the bounding box (red dotted rectangle). Scale bar = 250  $\mu$ m. (b) Summary of variability in "live" pixels (inversely proportional to nodal concentration) from the experimental design. Groups denoted by A, B, and C were significantly different from each other (p < 0.05). Both bioink viscosity and duration of ultrasonic actuation had significant effects on alignment of hASC in alginate

# 4.5. Study 5: Multilayered meniscus construct with circumferential hASC alignment fabricated via UABp

Figure 10 demonstrates the computational model outcomes and UABp of the meniscus-shaped construct with circumferentially-aligned hASC. The series of top views of the octagonal chamber from the COMSOL model represent the expected BAW nodal pattern in different regions of the construct when each transducer is actuated. The pressure nodes are most pronounced in front of each actuated transducer, but weaker patterns resulting from the effects of non-uniform transducer compliance and reflections manifest in surrounding regions of the chamber. Serial actuation of the transducers while bioprinting following the biomodeled toolpath would be expected to result in circumferential alignment along the semilunar construct. The peak acoustic pressure at the primary BAW nodes in this actuated chamber (1.5 MHz-200 mVpp) was 300 kPa, which was similar in magnitude to the peak pressure observed in the 2 MHz-200 mVpp group (250 kPa) in Study 2 wherein 100% cell viability was noted. In contrast, the peak pressure in the 1.5 MHz-200 mVpp group in Study 2 was 1600 kPa. This difference in peak pressures, given the same ultrasound actuation parameters, is a result of the difference in the transducer-reflector separation distance between the two chambers – L = 75 mm and 21 mm for the octagonal and rectangular chambers, respectively.

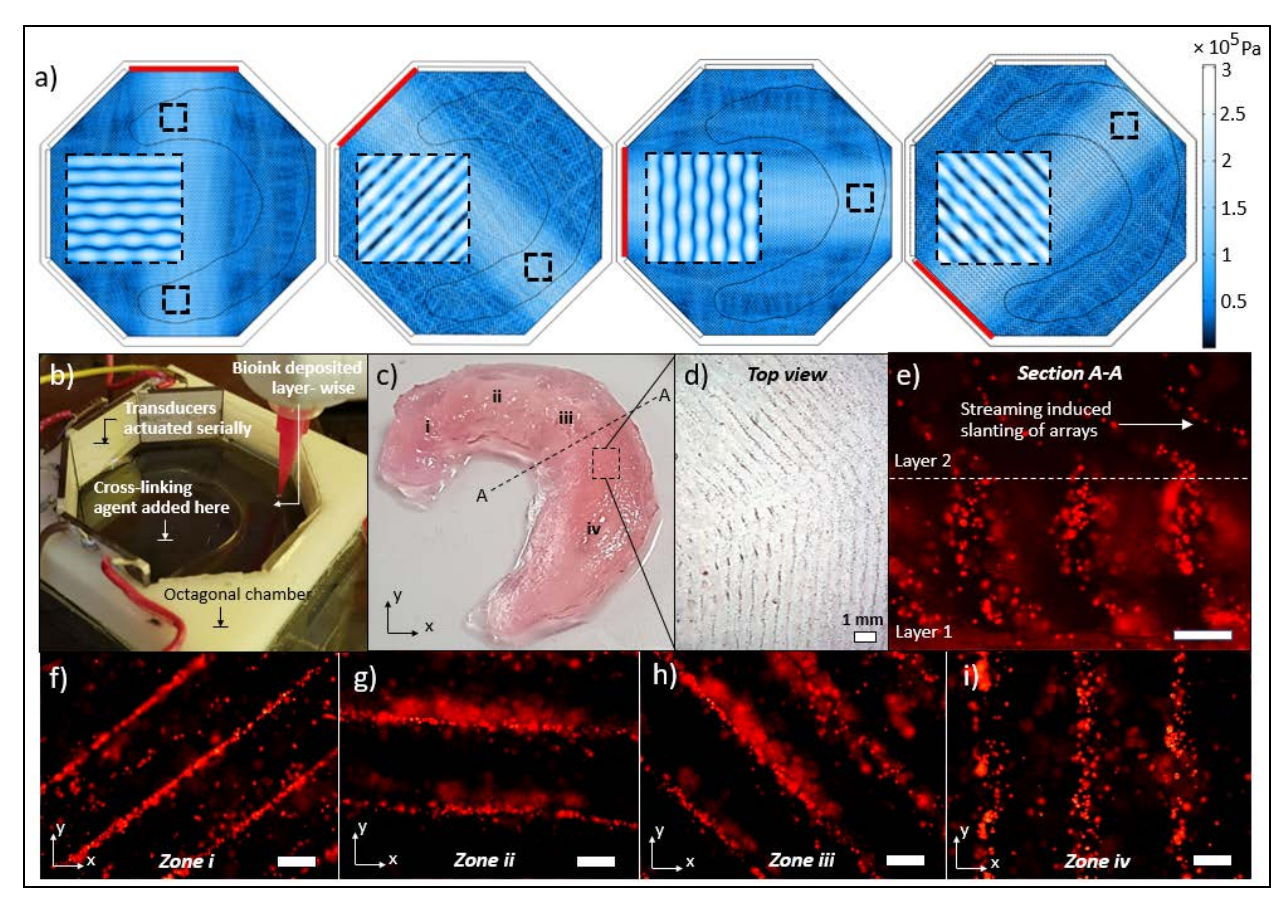


**Figure 10.** Computational modeling and UABp of a biomodeled knee meniscus construct featuring circumferentially aligned cells. (a) COMSOL models depicting the BAW nodal pattern in the octagonal chamber resulting from the actuation of each transducer (red), one at a time. The serial actuation of the four transducers would lead to a circumferential BAW pattern in the outlined semilunar construct. (b)

Alginate-hASC bioink being bioprinted following the biomodelled tool path into the octagonal chamber with the four transducers actuated serially (switching time of 1 s) to align cells prior to crosslinking. (c) The bioprinted construct, and (d) a dissection microscope image depicting the transition of alignment orientation of neutral red-stained viable hASC along adjacent faces of the octagonal chamber. (e) Cross-sectional image depicting hASC alignment across multiple layers along the construct thickness. (f-i) Representative fluorescence images highlighting four regions with differing cell alignment directions. All images were captured with the same x-y reference axes. Scale bar =  $250 \mu m$ .

The circumferential alignment was corroborated by the experimental results. Figure 10c shows the meniscus construct fabricated via UABp, and the fluorescence images of the top view (figure 10f-i) depict neutral red-stained viable hASC clustering along nodal planes parallel to the individual transducers. Of note, the dissection microscope image (figure 10d) shows the region of alignment transition resulting from adjacent transducers along the octagonal chamber. The cross-section image (figure 10e) highlights the slanting of cellular arrays along the construct thickness induced by viscous streaming resulting from the equivalent of burst mode actuation wherein the fluid is abruptly thrusted away from the transducer every time it is actuated for 1 s before the actuation is transferred to the adjacent transducer. An increasing slanting of arrays with increasing z-height is indicative of the non-uniform pressure field across the transducer surface (figures 5b) with greater compliance near the center of the transducer compared to its bottom periphery (figure S2).

#### 5. Discussion

Tissues are primarily composed of cells and ECM, and their organization is vital to the tissue function. Cells secrete the ECM proteins and constantly remodel and organize them to achieve tissue-specific function while the ECM guides the cell morphology and their behavior [1,5,7]. In engineering tissues for therapeutic applications, biomimicry of this microstructural organization is imperative. Given this symbiotic relationship between cells and ECM, multiple tissue engineering strategies are being investigated to achieve this. Contact guidance strategies wherein topographical features or scaffold fibers instruct the cellular migration, orientation, and subsequent ECM formation along the topographical boundaries or inter-fiber channels have been well-demonstrated in micro/nano-patterned substrates as well as in electrospun and 3D printed scaffolds [66–71]. Alternative strategies have involved the use of acoustophoretic, electrophoretic, photophoretic, magnetophoretic and chemotactic principles for patterning of suspended cells within bioinks without topographical stimuli [30-39].

The UAB process that is the focus of this work utilizes ultrasonic BAW for manipulation of cells into physiologically relevant patterns in 3D hydrogel constructs in contrast to many prior acoustophoretic approaches that have utilized SAW generated via a vibrating bottom substrate, primarily in the microfluidics domain [30,40,43]. Attenuation of the SAW amplitude as we move away from the vibrating substrate constrains the ability to effectively manipulate cells in 3D in viscous materials, thereby limiting the scalability of SAW-based approaches for creating constructs of physiologically relevant thicknesses. In comparison, BAW can be propagated laterally into bulk viscous bioinks, thereby enabling cell maneuverability across the thickness of 3D constructs (figure S4a). Furthermore, UAB utilizes an open-top chamber design, which allows its integration into bioprinting, thereby enabling the creation of single and multi-layered constructs with patient and tissue-specific geometries (figure S4b). This represents an advantage over most

other SAW and BAW-based patterning approaches that require closed chamber designs. This work maps out the UAB process, characterizing the relationships between the acoustical and bioink parameters and the resulting structural patterns and viability and metabolic activity of the cells.

It is of utmost importance that the viability of cells not be adversely affected by the biofabrication process. The UAB characterization results show that only a sub-set of acoustical parameter combinations are not optimal in this regard. The viability of hASC was 100% at the extreme groups in the mapped process space (0.71 MHz-100 mVpp and 2 MHz-200 mVpp), and their metabolic activities remained unchanged over 4 days. However, moderate frequencies (1 MHz and 1.5 MHz) at high amplitude (200 mVpp) exhibited the largest acoustic radiation forces (figure 4) and the lowest viability (figure 6). Of note, the two 2 MHz groups that had 100% viability 3 h post-fabrication retained their alignment and viability over 4 days in culture (figure S3), which points to the robustness of the process, provided optimal parameters are used. In future, assessment of the interplay between moderate frequencies at higher amplitudes and the resulting streaming on cell viability and metabolic activity over prolonged intervals in adherent bioink matrices is warranted to determine if the cells can recover from the immediate stresses encountered during UAB manipulation.

One of the primary contributions of this work includes the corroboration of the underlying theory governing the alignment of cells suspended in the bioink using ultrasound. Results show that the alignment characteristics of the hASC arrays can be controlled via the acoustical parameters. The spacing between adjacent arrays of clustered cells (figure 7) (analogous to "inter-fiber spacing" in scaffolds) tallies with the theoretical spacing between adjacent pressure nodes (table 1), and it is inversely proportional to the applied frequency. Furthermore, at a given frequency, the concentration of cells clustering along the pressure nodal planes (analogous to "fiber width" in scaffolds) is directly proportional to the frequency and voltage amplitude actuating the transducer (figure 7) and the actuation duration (figure 9) and inversely proportional to the bioink viscosity (figure 9). For example, at the 2 MHz frequency, the average width of the cellular arrays formed in the low viscosity bioink with 200 mVpp actuation for 20 min was 50  $\mu$ m, in contrast to the average width of 65  $\mu$ m and 108  $\mu$ m noted in the high viscosity ink with 200 mVpp for 10 min and 100 mVpp for 20 min, respectively.

The results of Studies 1-4 taken together signify that while using UAB, optimization of at least four critical parameters – bioink viscosity, frequency, amplitude, and actuation duration – is necessary in order to create tissue-specific patterns of interest while maintaining the viability and metabolic activity of cells. By using the appropriate combinations of these parameters and bioink chamber designs with one or more transducer-reflector pairs, UAB provides the flexibility to produce controlled patterns of viable cells, which is a foremost step in creating engineered tissues with biomimetic ECM organization. In moving towards tissue-specific applications, additional relevant parameters that will need to be characterized include the frequency of the burst mode of actuation and the type of cells and their concentration in the bioink. We determined during pilot studies that burst mode actuation is critical to UAB because continuous actuation can adversely affect the transducer compliance characteristics over time. Continuous actuation also results in heat generation which can be detrimental to cells within the bioink. As such, the frequency of burst mode actuation can impact the UAB processing time, cell viability and fidelity of the alignment patterns within constructs. With regards to the cell type, the size, density, and compressibility of

cells will govern the radiation and drag forces that they experience, which in turn will dictate their alignment characteristics and functional responses to ultrasound. In addition to the characterization of a more comprehensive set of cellular, bioink and acoustical parameters and bioink chamber design to achieve high fidelity, high viability, tissue-specific patterns of interest, the UAB process (and its adaptations) can be further enhanced by optimizing the transducer design and constitution. From the hydrophone experiments, it was evident that the commercial transducers used in this study underwent a non-uniform surface deformation that resulted in a non-uniform pressure field across its surface (figure 5b). This resulted in perturbations induced by turbulent streams (figure S2b) that were observably higher at low to moderate frequencies. By exploring appropriate piezo material properties, impedance matching and in-process cooling strategies, uniform transducer compliance along its surface resulting in more uniform BAW generation (figure S2a) can be achieved. This would help reduce the perturbations, thereby improving the cell viability. This would also help linearize the currently scalloped profile of cell arrays along the nodal planes and improve the pattern fidelity.

Another important contribution of this work is the demonstration of the UABp process that allows biomimicry at multiple length scales. Although 3D meniscal scaffolds have been investigated before, Study 5 illustrates the ability to bioprint a multi-layered medial knee meniscus construct with patient-specific macro-geometry and tissue-specific micro-architectural patterns of viable cells. This construct was bioprinted with the 200 cP alginate formulation. We would like to note that although alginate bioinks of 5 cP, 70 cP and 200 cP used across the five studies in this paper are all bioprintable through synergistic extrusion and chemical crosslinking, the 200 cP formulation leads to constructs with better fidelity of patient-specific macro-geometry while still allowing the ultrasound-assisted patterning of cells. Following up on this work, future studies can investigate the maturation of such aligned meniscus constructs under appropriate culturing conditions to achieve tissue-specific cellular differentiation, ECM formation, and functionallycritical biomechanical properties. Furthermore, in addition to extrusion bioprinting, the UAB patterning principle can be extended to other forms of bioprinting including inkjet, laser-assisted, DLP and SLA-based techniques. Through astute bioink and process design and optimization, an extensive gambit of cellular patterns, for example, crisscross configuration in connective tissues or radial arrangement of hepatocytes in hepatic lobules, coupled with integration of multiple cell types in each layer is conceivable with UABp.

By successfully demonstrating 3D cell patterning in viscous hydrogels and mapping the process-structure relationships to achieve controllable micro-architecture and high cell viability, this study has established the foundation for creating biomimetic 3D tissues using UAB. Future studies will focus on UAB-based patterning of application-specific cell lines while investigating the bioink properties, inter-array spacing, and nodal concentrations to guide cellular morphology [72], differentiation [73] and intercellular signaling [74] to produce ECM that matches the hierarchical fibrous structure of mammalian tissues. With UAB, a non-reliance on chemotactic or physical cues for creating ECM alignment and a possibility of scalability and flexibility takes us a step closer to creating functional therapeutic engineered tissue substitutes.

#### 6. Conclusion

In this work, we have investigated the process of patterning cells in hydrogel matrices using longitudinal BAW via a new UAB platform design using computational modeling and experimental

designs. The multiphysics model highlighted the effects of frequency and source signal amplitude on the acoustic pressure distribution, which were corroborated by hydrophone pressure field measurements and the alignment characteristics of hASC arrays observed in the experimental studies. The experimental studies show that the bioink viscosity, frequency, amplitude, and actuation duration, and especially their interactions, impact the cell viability and alignment characteristics. Of note: 1) the combinations of moderate frequency and high amplitude adversely affect cell viability, 2) the inter-array spacing is inversely proportional to the frequency, and 3) the nodal concentration is directly proportional to the amplitude and actuation duration and inversely proportional to the bioink viscosity. The 3D bioprinting of a knee meniscus construct using an adaptation of UAB with circumferential cell alignment across multiple layers was also demonstrated in this work. Through the five studies, we have mapped out the process-structure relationships in UAB and discussed how the process design and fidelity of resulting patterned constructs can be enhanced moving forward. Future studies will focus on investigating the effects of the UAB process parameters and cellular patterns on the organization and mechanical anisotropy of ECM secreted by patterned cells.

## Acknowledgements

The authors would like to gratefully acknowledge the support from the US NSF (CMMI#1652489) and thank Dr. Omer Oralkan and Jeanne Lunsford Sanders (NC State University, Department of Electrical and Computer Engineering) for assistance with hydrophone testing. A patent is pending on the disclosed subject matter (US 62747789).

#### References

- [1] Bourget J-M, A. F, Guillemette M, Veres T and Germain L 2013 Alignment of Cells and Extracellular Matrix Within Tissue- Engineered Substitutes *Advances in Biomaterials Science and Biomedical Applications* (InTech) pp 365–90
- [2] Kielty C M and Grant M E 2002 The Collagen Family: Structure, Assembly, and Organization in the Extracellular Matrix *Connective Tissue and Its Heritable Disorders* (Hoboken, NJ, USA: John Wiley & Sons, Inc.) pp 159–221
- [3] Frantz C, Stewart K M and Weaver V M 2010 The extracellular matrix at a glance. *J. Cell Sci.* **123** 4195–200
- [4] Badylak S F 2007 The extracellular matrix as a biologic scaffold material *Biomaterials* **28** 3587–93
- [5] Kjær M 2004 Role of Extracellular Matrix in Adaptation of Tendon and Skeletal Muscle to Mechanical Loading *Physiol. Rev.* **84** 649–98
- [6] Screen H R C, Berk D E, Kadler K E, Ramirez F and Young M F 2015 Tendon functional extracellular matrix. *J. Orthop. Res.* **33** 793–9
- [7] Birch H L, Thorpe C T and Rumian A P 2013 Specialisation of extracellular matrix for function in tendons and ligaments. *Muscles. Ligaments Tendons J.* **3** 12–22
- [8] Makris E A, Hadidi P and Athanasiou K A 2011 The knee meniscus: Structure–function, pathophysiology, current repair techniques, and prospects for regeneration *Biomaterials* **32** 7411–31
- [9] Andrews S H J, Rattner J B, Abusara Z, Adesida A, Shrive N G and Ronsky J L 2014 Tie-fibre structure and organization in the knee menisci. *J. Anat.* **224** 531–7
- [10] Purslow P P 2008 The Extracellular Matrix of Skeletal and Cardiac Muscle *Collagen* (Boston, MA: Springer US) pp 325–57
- [11] Bursac N, Parker K K, Iravanian S and Tung L 2002 Cardiomyocyte Cultures With

- Controlled Macroscopic Anisotropy A Model for Functional Electrophysiological Studies of Cardiac Muscle *Circ. Res.* **91** e45–54
- [12] Meek K M and Boote C 2004 The organization of collagen in the corneal stroma *Exp. Eye Res.* **78** 503–12
- [13] Linda J M, Pels L and Vrensen G F J M 1995 *Investigative Ophthalmology & Visual Science* vol 36 ([Association for Research in Vision and Ophthalmology, etc.])
- [14] Hoehme S, Brulport M, Bauer A, Bedawy E, Schormann W, Hermes M, Puppe V, Gebhardt R, Zellmer S, Schwarz M, Bockamp E, Timmel T, Hengstler J G and Drasdo D 2010 Prediction and validation of cell alignment along microvessels as order principle to restore tissue architecture in liver regeneration. *Proc. Natl. Acad. Sci. U. S. A.* **107** 10371–6
- [15] Klaas M, Kangur T, Viil J, Mäemets-Allas K, Minajeva A, Vadi K, Antsov M, Lapidus N, Järvekülg M and Jaks V 2016 The alterations in the extracellular matrix composition guide the repair of damaged liver tissue *Sci. Rep.* **6** 27398
- [16] Chiu J-J, Chen L-J, Chen C-N, Lee P-L and Lee C-I 2004 A model for studying the effect of shear stress on interactions between vascular endothelial cells and smooth muscle cells *J. Biomech.* **37** 531–9
- [17] Wagenseil J E and Mecham R P 2009 Vascular extracellular matrix and arterial mechanics. *Physiol. Rev.* **89** 957–89
- [18] Bitar K N, Raghavan S and Zakhem E 2014 Tissue Engineering in the Gut: Developments in Neuromusculature *Gastroenterology* **146** 1614–24
- [19] Meran L, Baulies A and Li V S W 2017 Intestinal Stem Cell Niche: The Extracellular Matrix and Cellular Components *Stem Cells Int.* **2017** 1–11
- [20] Abrams G D, Frank R M, Gupta A K, Harris J D, McCormick F M and Cole B J 2013 Trends in Meniscus Repair and Meniscectomy in the United States, 2005-2011 *Am. J. Sports Med.* **41** 2333–9
- [21] Yelin E, Weinstein S and King T 2016 The burden of musculoskeletal diseases in the United States *Semin. Arthritis Rheum.* **46** 259–60
- [22] Lohmander L S, Englund P M, Dahl L L and Roos E M 2007 The Long-term Consequence of Anterior Cruciate Ligament and Meniscus Injuries *Am. J. Sports Med.* **35** 1756–69
- [23] De Bruycker M, Verdonk P C M and Verdonk R C 2017 Meniscal allograft transplantation: a meta-analysis. *SICOT-J* **3** 1–15
- [24] Lohmander L S, Östenberg A, Englund M and Roos H 2004 High prevalence of knee osteoarthritis, pain, and functional limitations in female soccer players twelve years after anterior cruciate ligament injury *Arthritis Rheum.* **50** 3145–52
- [25] Salmon L J, Russell V J, Refshauge K, Kader D, Connolly C, Linklater J and Pinczewski L A 2006 Long-term Outcome of Endoscopic Anterior Cruciate Ligament Reconstruction with Patellar Tendon Autograft *Am. J. Sports Med.* **34** 721–32
- [26] Moroni L, Boland T, Burdick J A, De Maria C, Derby B, Forgacs G, Groll J, Li Q, Malda J, Mironov V A, Mota C, Nakamura M, Shu W, Takeuchi S, Woodfield T B F, Xu T, Yoo J J and Vozzi G 2018 Biofabrication: A Guide to Technology and Terminology. *Trends Biotechnol.* **36** 384–402
- [27] Starly B and Shirwaiker R A 2015 Three-dimensional Bioprinting. Chapter 3 in 3D Bioprinting and Nanotechnology in Tissue Engineering and Regenerative Medicine, Eds. L. Zhang, J. P. Fisher, and K. Leong, Academic Press, Waltham, MA
- [28] Woodfield T, Lim K, Morouço P, Levato R, Malda J and Melchels F 2017 5.14 Biofabrication in Tissue Engineering *Compr. Biomater. II* 236–66
- [29] Groll J, Boland T, Blunk T, Burdick J A, Cho D-W, Dalton P D, Derby B, Forgacs G, Li Q, Mironov V A, Moroni L, Nakamura M, Shu W, Takeuchi S, Vozzi G, Woodfield T B F, Xu T, Yoo J J and Malda J 2016 Biofabrication: reappraising the definition of an evolving field

- Biofabrication 8 013001
- [30] Shi J, Ahmed D, Mao X, Lin S-C S, Lawit A and Huang T J 2009 Acoustic tweezers: patterning cells and microparticles using standing surface acoustic waves (SSAW) *Lab Chip* **9** 2890
- [31] Drinkwater B W 2016 Dynamic-field devices for the ultrasonic manipulation of microparticles *Lab Chip* **16** 2360–75
- [32] Park K, Suk H-J, Akin D and Bashir R 2009 Dielectrophoresis-based cell manipulation using electrodes on a reusable printed circuit board *Lab Chip* **9** 2224
- [33] Hunt T P and Westervelt R M 2006 Dielectrophoresis tweezers for single cell manipulation *Biomed. Microdevices* **8** 227–30
- [34] Pirlo R K, Ma Z, Sweeney A, Liu H, Yun J X, Peng X, Yuan X, Guo G X and Gao B Z 2011 Laser-guided cell micropatterning system *Rev. Sci. Instrum.* **82** 013708
- [35] Ma Z, Liu Q, Liu H, Yang H, Yun J X, Xu M, Eisenberg C A, Borg T K, Markwald R and Gao B Z 2012 Cardiogenic Regulation of Stem-Cell Electrical Properties in a Laser-Patterned Biochip *Cell. Mol. Bioeng.* **5** 327–36
- [36] Liu W, Dechev N, Foulds I G, Burke R, Parameswaran A and Park E J 2009 A novel permalloy based magnetic single cell micro array *Lab Chip* **9** 2381
- [37] Tsunehisa Kimura \*,†,‡, Yukiko Sato †, Fumiko Kimura ‡,§, Masakazu Iwasaka § and ueno§ S 2004 Micropatterning of Cells Using Modulated Magnetic Fields
- [38] Zhang S, Yan L, Altman M, Lässle M, Nugent H, Frankel F, Lauffenburger D A, Whitesides G M and Rich A 1999 Biological surface engineering: a simple system for cell pattern formation *Biomaterials* **20** 1213–20
- [39] Scotchford C A, Gilmore C P, Cooper E, Leggett G J and Downes S 2002 Protein adsorption and human osteoblast-like cell attachment and growth on alkylthiol on gold self-assembled monolayers *J. Biomed. Mater. Res.* **59** 84–99
- [40] Franke T, Braunmüller S, Schmid L, Wixforth A and Weitz D A 2010 Surface acoustic wave actuated cell sorting (SAWACS) *Lab Chip* **10** 789
- [41] Myeong Chan Jo M C and Guldiken R 2011 A label-free cell separation using surface acoustic waves 2011 Annual International Conference of the IEEE Engineering in Medicine and Biology Society vol 2011 (IEEE) pp 7691–4
- [42] Shilton R, Tan M K, Yeo L Y and Friend J R 2008 Particle concentration and mixing in microdrops driven by focused surface acoustic waves *J. Appl. Phys.* **104** 014910
- [43] Guo F, Mao Z, Chen Y, Xie Z, Lata J P, Li P, Ren L, Liu J, Yang J, Dao M, Suresh S and Huang T J 2016 Three-dimensional manipulation of single cells using surface acoustic waves. *Proc. Natl. Acad. Sci. U. S. A.* **113** 1522–7
- [44] Barani A, Paktinat H, Janmaleki M, Mohammadi A, Mosaddegh P, Fadaei-Tehrani A and Sanati-Nezhad A 2016 Microfluidic integrated acoustic waving for manipulation of cells and molecules *Biosens. Bioelectron.* **85** 714–25
- [45] Qiu Y, Wang H, Demore C E M, Hughes D A, Glynne-Jones P, Gebhardt S, Bolhovitins A, Poltarjonoks R, Weijer K, Schönecker A, Hill M and Cochran S 2014 Acoustic devices for particle and cell manipulation and sensing. *Sensors (Basel)*. **14** 14806–38
- [46] Friend J and Yeo L Y 2011 Microscale acoustofluidics: Microfluidics driven via acoustics and ultrasonics *Rev. Mod. Phys.* **83** 647–704
- [47] Bouyer C, Chen P, Güven S, Demirtaş T T, Nieland T J F, Padilla F and Demirci U 2016 A Bio-Acoustic Levitational (BAL) Assembly Method for Engineering of Multilayered, 3D Brain-Like Constructs, Using Human Embryonic Stem Cell Derived Neuro-Progenitors *Adv. Mater.* **28** 161–7
- [48] Chen P, Güven S, Usta O B, Yarmush M L and Demirci U 2015 Biotunable Acoustic Node Assembly of Organoids *Adv. Healthc. Mater.* **4** 1937–43
- [49] Garvin K A, Dalecki D and Hocking D C 2011 Vascularization of Three-Dimensional Collagen Hydrogels Using Ultrasound Standing Wave Fields *Ultrasound Med. Biol.* **37**

- 1853-64
- [50] Axpe E, Oyen M, Axpe E and Oyen M L 2016 Applications of Alginate-Based Bioinks in 3D Bioprinting *Int. J. Mol. Sci.* **17** 1976
- [51] Andersen T, Strand B L, Formo K, Alsberg E and Christensen B E 2011 Alginates as biomaterials in tissue engineering *Carbohydrate Chemistry: Chemical and Biological Approaches* ed A P Rauter and T K Lindhorst (RSC Publications) pp 227–58
- [52] Zuk P A, Zhu M, Mizuno H, Huang J, Futrell J W, Katz A J, Benhaim P, Lorenz H P and Hedrick M H 2001 Multilineage Cells from Human Adipose Tissue: Implications for Cell-Based Therapies *Tissue Eng.* **7** 211–28
- [53] Pak J, Lee J H and Lee S H 2014 Regenerative repair of damaged meniscus with autologous adipose tissue-derived stem cells. *Biomed Res. Int.* **2014** 436029
- [54] Ruiz-Ibán M Á, Díaz-Heredia J, García-Gómez I, Gonzalez-Lizán F, Elías-Martín E and Abraira V 2011 The Effect of the Addition of Adipose-Derived Mesenchymal Stem Cells to a Meniscal Repair in the Avascular Zone: An Experimental Study in Rabbits *Arthrosc. J. Arthrosc. Relat. Surg.* **27** 1688–96
- [55] Narayanan L K, Huebner P, Fisher M B, Spang J T, Starly B, Shirwaiker R A and Fitts E P 2016 3D-Bioprinting of Polylactic Acid (PLA) Nanofiber–Alginate Hydrogel Bioink Containing Human Adipose-Derived Stem Cells *ACS Biomater. Sci. Eng.* **2** 1732–42
- [56] Toratani T, Nakase J, Numata H, Oshima T, Takata Y, Nakayama K and Tsuchiya H 2017 Scaffold-Free Tissue-Engineered Allogenic Adipose-Derived Stem Cells Promote Meniscus Healing *Arthrosc. J. Arthrosc. Relat. Surg.* **33** 346–54
- [57] Cengiz I F, Pereira H, de Girolamo L, Cucchiarini M, Espregueira-Mendes J, Reis R L and Oliveira J M 2018 Orthopaedic regenerative tissue engineering en route to the holy grail: disequilibrium between the demand and the supply in the operating room. *J. Exp. Orthop.* **5** 14
- [58] Qi Y, Yang Z, Ding Q, Zhao T, Huang Z and Feng G 2016 Targeted transplantation of iron oxide-labeled, adipose-derived mesenchymal stem cells in promoting meniscus regeneration following a rabbit massive meniscal defect. *Exp. Ther. Med.* **11** 458–66
- [59] Yosioka K and Kawasima Y 1955 Acoustic radiation pressure on a compressible sphere Acta Acust. united with Acust. **5** 167–73
- [60] Settnes M and Bruus H 2012 Forces acting on a small particle in an acoustical field in a viscous fluid *Phys. Rev. E* **85** 016327
- [61] Collinson C D and Roper T 1995 Stokes Drag *Particle mechanics* (Butterworth-Heinemann) p 30
- [62] Barnkob R, Augustsson P, Laurell T and Bruus H 2010 Measuring the local pressure amplitude in microchannel acoustophoresis *Lab Chip* **10** 563
- [63] Scholz M-S, Drinkwater B W, Llewellyn-Jones T M and Trask R S 2015
  Counterpropagating wave acoustic particle manipulation device for the effective
  manufacture of composite materials *IEEE Trans. Ultrason. Ferroelectr. Freq. Control* **62**1845–55
- [64] Slotwinski J 2002 Ultrasonics Testing *Handbook of Reference Data for Nondestructive Testing* ed L Mordfin (ASTM International) pp 31–48
- [65] StemInc 2017 Piezo Material Properties Online: https://www.steminc.com/PZT/en/piezo-materials-properties
- [66] Mauck R L, Baker B M, Nerurkar N L, Burdick J A, Li W-J, Tuan R S and Elliott D M 2009 Engineering on the Straight and Narrow: The Mechanics of Nanofibrous Assemblies for Fiber-Reinforced Tissue Regeneration *Tissue Eng. Part B Rev.* **15** 171–93
- [67] Lee C H, Shin H J, Cho I H, Kang Y-M, Kim I A, Park K-D and Shin J-W 2005 Nanofiber alignment and direction of mechanical strain affect the ECM production of human ACL fibroblast *Biomaterials* **26** 1261–70
- [68] Warren PB, Huebner P, Spang JT, Shirwaiker RA and Fisher MB 2017 Engineering

- 3D-Bioplotted scaffolds to induce aligned extracellular matrix deposition for musculoskeletal soft tissue replacement *Connect. Tissue Res.* **58** 342–54
- [69] Manwaring M E, Walsh J F and Tresco P A 2004 Contact guidance induced organization of extracellular matrix *Biomaterials* **25** 3631–8
- [70] Stevens M M and George J H 2005 Exploring and engineering the cell surface interface. *Science* **310** 1135–8
- [71] Aubin H, Nichol J W, Hutson C B, Bae H, Sieminski A L, Cropek D M, Akhyari P and Khademhosseini A 2010 Directed 3D cell alignment and elongation in microengineered hydrogels *Biomaterials* **31** 6941–51
- [72] Chen C S, Mrksich M, Huang S, Whitesides G M and Ingber D E 1997 Geometric control of cell life and death. *Science* **276** 1425–8
- [73] Burdick J A and Vunjak-Novakovic G 2009 Engineered Microenvironments for Controlled Stem Cell Differentiation *Tissue Eng. Part A* **15** 205–19
- [74] Nelson C M and Chen C S 2002 Cell-cell signaling by direct contact increases cell proliferation via a PI3K-dependent signal *FEBS Lett.* **514** 238–42